

Properties of Galaxies with Counter-rotating Stellar Disks in the MaNGA Survey

MIN BAO ^{1,2} ZHENYU TANG,^{1,2,*} YANMEI CHEN ^{1,2,†} YONG SHI ³ AND QIUSHENG GU ^{1,2}

¹*School of Astronomy and Space Science, Nanjing University, Nanjing 210023, China*

²*Key Laboratory of Modern Astronomy and Astrophysics (Nanjing University), Ministry of Education, Nanjing 210023, China*

³*Department of Astronomy, Westlake University, Hangzhou 310030, Zhejiang Province, China*

ABSTRACT

Gas accretion process can fuel both star formation and black hole activity, playing a critical role in galaxy evolution. The counter-rotating structures are believed to originate from gas accretion, serving as an ideal laboratory for studying its impact on galaxy evolution. Based on the Mapping Nearby Galaxies at Apache Point Observatory (MaNGA) survey, we built a sample of 147 galaxies with counter-rotating stellar disks (CRDs). This is the largest CRD sample to date, accounting for $\sim 1.5\%$ of the MaNGA survey. For a subset of 138 CRDs, global stellar mass (M_*) and star formation rate (SFR) were measured in reference. We constructed a control sample with similar M_* and SFR but lacking counter-rotating structures. The CRDs relatively exhibit more bulge-dominated morphology, lower molecular gas mass fraction and reside in less dense environment, supporting the hypothesis that they primarily originate from gas accretion. We classified 96 out of 138 CRDs into four types based on their stellar and gas kinematics following the criteria from Bao et al. (2022). There are two additional CRD types: 8 CRDs show misalignment between both stellar disks and gas disk, indicating multiple gas accretion events with differing angular momentum directions; 34 CRDs lack ionized gas emission, showing the highest M_* among all the CRD types, which may represent a final stage of CRD evolution. We compared the radial gradients of gas-phase metallicity and stellar population properties between CRD types, and found that the impact of gas accretion on galaxy evolution primarily depends on the abundance of pre-existing gas in progenitors.

Keywords: galaxies: kinematics and dynamics — galaxies: evolution

1. INTRODUCTION

In the Λ CDM cosmology, the first structure formed in the Universe is the dark matter halo (Blumenthal et al. 1984). Subsequently, baryons fall into the potential well of dark matter halo, assembling galaxy (Fall & Efstathiou 1980). Gas accretion (Conselice & Arnold 2009; Kauffmann et al. 2010; Tillson et al. 2011) and galaxy merger (Diemand et al. 2007) are the primary mechanisms for galaxy assembly. The former involves the smooth accretion of external gas, while the latter refers to the merging with other galaxies. Wang et al. (2011) investigated the assembly history of Milky Way-mass dark matter haloes using Aquarius simulation series, confirming that the majority of baryons from which galaxies form are acquired through external accretion rather than mergers. L’Huillier et al. (2012) employed a multi-zoom simulation to study the formation of 530 galaxies, and found that the average fraction of mass assembled by gas accretion is $\sim 77\%$, indicating that gas accretion dominates galaxy assembly.

Indirect evidences of gas accretion have been identified in H I observations of galaxies and their environments (Sancisi et al. 2008), such as: (1) a large number of galaxies being surrounded by H I-rich dwarfs or exhibiting H I tails; (2) significant amounts of extra-planar H I around nearby spiral galaxies; (3) extended and warped H I layers presenting in spiral galaxies; and (4) most H I disks showing morphological or dynamical asymmetries. However, gas accretion is not the only possible explanation for these features. Early observational studies aiming to directly confirm gas accretion were constrained by the sensitivity limitations of old radio telescopes (Morganti et al. 2009; Maccagni et al. 2014). With the development of radio telescopes, it is now possible to study gas accretion processes through H I emission

* Min Bao and Zhenyu Tang share first authorship.

† E-mail: chenym@nju.edu.cn.

lines in individual galaxies. For instance, [Santana et al. \(2025\)](#), using HI observations with high spatial resolution from MeerKAT, found that the HI in NGC 5643 extends beyond the stellar disk with morphological and kinematic asymmetries, and identified an extended 30 kpc tail with counter-rotating velocities on the northern side of the disk, providing direct evidence for HI gas accretion in this galaxy. Nevertheless, to date, such investigations of gas accretion processes remain limited to case studies of individual sources.

Kinematically misaligned galaxies, including gas-gas, gas-stellar or stellar-stellar components having different angular momentum (AM) directions, are widely believed to be products of gas accretion ([Corsini 2014](#)), serving as an ideal laboratory for studying its impact on galaxy evolution. The external gas can be accreted from gas-rich satellites ([Gasymov et al. 2025](#)) or the cosmic web ([Sánchez Almeida et al. 2014](#)). Due to the large collision cross-section of gas components, fewer than ten galaxies with gas-gas misalignment have been observed to date, with the majority detected by long-slit spectroscopy ([Braun et al. 1994](#); [Fisher et al. 1994](#); [Plana & Boulesteix 1996](#); [Hunter et al. 1999](#); [Corsini et al. 2002](#); [Cao et al. 2022](#)). Thanks to the development of large integral-field spectroscopy surveys, like ATLAS^{3D} ([Cappellari et al. 2011](#)), CALIFA ([Sánchez et al. 2012](#)) and SAMI ([Croom et al. 2012](#)), the phenomenon of gas-star misalignment was found to be ubiquitous in quiescent galaxies ([Davis et al. 2011](#); [Barrera-Ballesteros et al. 2015](#); [Ristea et al. 2022](#)). Meanwhile, samples of gas-star misalignment were also reported in star-forming galaxies ([Chen et al. 2016](#); [Jin et al. 2016](#); [Bryant et al. 2019](#)).

Galaxies with two counter-rotating stellar disks usually show two off-center but symmetric peaks along the major axis in the stellar velocity dispersion field, which is referred as 2σ feature in the literature. The co-existing blueshifted and redshifted absorption components at the interface of the two stellar disks contribute to the broadening of absorption lines. Several galaxy cases hosting counter-rotating stellar disks (CRDs) have been studied over the past three decades ([Rubin et al. 1992](#); [Coccatto et al. 2011, 2013](#); [Pizzella et al. 2014](#); [Katkov et al. 2016](#); [Mitzkus et al. 2017](#); [Pizzella et al. 2018](#)). In all these cases, the stellar disk which co-rotates with gas component is younger and has lower metallicity. Such trends support a formation scenario that the progenitor of CRDs accretes counter-rotating gas, fueling the formation of a new stellar disk which counter-rotates with the pre-existing one.

In statistic, [Bevacqua et al. \(2022\)](#) studied 64 galaxies with CRDs selected from ~ 4000 galaxies in the early data release of MaNGA survey, finding the incident rate for CRDs in MaNGA is $<5\%$ for ellipticals, $<3\%$ for lenticulars, and $<1\%$ for spirals. Through analysing the stellar populations of two stellar disks, they found the gas co-rotates with the younger disk in most cases, suggesting that CRDs form primarily via gas accretion in retrograde rotation with respect to the pre-existing stellar disk. [Bao et al. \(2022\)](#) studied 101 galaxies with CRDs from ~ 9500 MaNGA galaxies, classified these 101 galaxies into four types based on the features of their stellar and gas velocity fields. Under the assumption of the gas accretion formation mechanism, they propose that these distinct kinematic features are primarily dominated by two key factors, including (1) the abundance of pre-existing gas in the progenitor and (2) the efficiency in angular momentum consumption.

In this study, we build a sample of 147 CRDs from the final data release of MaNGA survey, which is the largest CRD sample to date. In Section 2, we introduce the MaNGA survey and sample selection. Based on their gas and stellar kinematics, we classify the CRD sample into six types. In Section 3, we analyze the global and spatially resolved properties of different types of CRDs, and make comparisons with their control samples. In Section 4, we discuss the corresponding formation scenarios for different types of CRDs. Finally, we summarize the conclusion in Section 5.

2. DATA

2.1. MaNGA survey

As one of the three core programs in the fourth-generation Sloan Digital Sky Survey (SDSS-IV; [Blanton et al. 2017](#)), MaNGA observed 10,010 unique galaxies with redshift coverage of $z \sim [0.01, 0.15]$ and flat stellar mass distribution in a range of $\log(M_*/M_\odot) \sim [9, 11]$ ([Wake et al. 2017](#); [Abdurro'uf et al. 2022](#)). Using the Baryon Oscillation Spectroscopic Survey (BOSS) spectrographs ([Smee et al. 2013](#)) on the 2.5-meter telescope at the Apache Point Observatory ([Gunn et al. 2006](#)), MaNGA employed dithered observations using integral field spectroscopy (IFS; [Drory et al. 2015](#)), with diameter ranging from $12''$ (19 fibers) to $32''$ (127 fibers). Two dual-channel BOSS spectrographs provided wide wavelength coverage of $\lambda \sim [3600, 10, 300] \text{ \AA}$, with a median spectral resolution of $R \sim 2000$.

The data products in this study are obtained from the final data release of MaNGA survey. For each MaNGA galaxy, the global stellar mass and star formation rate are obtained from [Chang et al. \(2015\)](#), which are estimated through spectral energy distribution (SED) fitting combining SDSS and WISE photometry. We refer to Figures 3 and 5 of [Chang et al. \(2015\)](#) for example SED fitting results of massive, quiescent galaxies and blue, star-forming galaxies. The

bulge-to-total ratio (B/T) is gathered from the MaNGA PyMorph DR17 photometric catalog (Fischer et al. 2019), derived through Sérsic + Exponential fitting to the 2D surface brightness profile of SDSS image using PYMORPH. Other global properties, including photometric position angle (ϕ), effective radius (Re) and axial ratio (b/a) are extracted from NASA-Sloan Atlas catalog (NSA, Blanton et al. 2011), based on one-component, two-dimensional Sérsic fitting. The spatially resolved light-weighted stellar metallicity ($[Z/H]$) is provided by the pyPipe3D pipeline (Sánchez et al. 2022), which serves as a proxy for the metal enrichment cycle. This quantity is derived by fitting the stellar continuum with simple stellar population (SSP) models. Other spatially resolved properties, including emission line flux, gas (or stellar) velocity and velocity dispersion, 4000 Å break (D_n4000) defined as the flux ratio between two narrow bands of 3850-3950 Å and 4000-4100 Å, are obtained from MaNGA data analysis pipeline (DAP, Westfall et al. 2019).

DAP is a survey-led software package for analysing the spatially resolved MaNGA spectra to generate high-level data products. It performs two full-spectrum fittings for each spectrum with g -band signal-to-noise ratio (S/N) higher than 1, both using penalized pixel-fitting (pPXF; Cappellari 2017), but with different templates. The templates used to determine the stellar kinematics are from MILESHC (Sánchez-Blázquez et al. 2006), and the templates used to fit the stellar continuum during the emission-line fitting module are from MASTARSSP (Yan et al. 2019). MILESHC/MASTARSSP is a stellar-template library constructed by hierarchically-clustering the MILES/MaStar stellar library. In the first full-spectrum fitting, the stellar continuum is modeled as a linear combination of MILESHC templates, convolved with the line-of-sight velocity distribution (LOSVD; Cappellari & Emsellem 2004; Mitzkus et al. 2017), to determine the stellar kinematics. The first two moments of the LOSVD correspond to velocity and velocity dispersion of stellar component. In the second full-spectrum fitting, all the emission lines are simultaneously modeled by Gaussian profiles using pPXF. Each emission line can be modeled as a Gaussian profile characterized by its flux, line center and width, with all the emission line centers tied together in the velocity space. The velocity and velocity dispersion of gas component are then derived from the modeled line center and width.

2.2. The CRD sample

CRDs exhibit one or both of the following characteristics: (1) the presence of 2σ feature in the stellar velocity dispersion (σ_*) field; (2) the clear counter-rotation (with position angle offset higher than 150°) between inner and outer stellar disks in the stellar velocity (v_*) field. The upper panels of Figure 1 display an example of CRDs with 2σ feature. Figure 1(a) displays the σ_* field in polar coordinate, with the black solid and dashed lines representing the photometric major and minor axes. The upper half of minor axis is set as $\theta = 0^\circ$, with increasing value of θ in the counter-clockwise direction. To analyze the σ_* distribution, we divide the σ_* field into circular sectors with a sector width of $\Delta\theta = 5^\circ$. Figure 1(b) shows the σ_* as a function of θ , with the peak value normalized to 1. The black circle represents the median σ_* in each sector, and the error bar shows the $\pm 1\sigma$ scattering range. To search for the σ_* enhanced region, we fit these black circles with a double-Gaussian model using the Python-based package CURVE_FIT. The black profile in Figure 1(b) is the best-fitting Gaussian model. The two peaks locate at $\theta_1 = 101.5 \pm 1.6^\circ$ and $\theta_2 = 272.0 \pm 1.7^\circ$, marked by the vertical blue lines. We select 1267 candidates satisfying $|\theta_1 - 90^\circ| \leq \theta_c$ and $|\theta_2 - 270^\circ| \leq \theta_c$, where $\theta_c = 50^\circ$. This criterion ensures that the 2σ feature is located around the major axis. Through visual inspection, we exclude candidates with galaxy pair within the same MaNGA field-of-view, ongoing merger, galaxies with irregular morphology, or non-smooth σ_* pattern, leaving 135 CRDs exhibiting 2σ feature.

The lower panels of Figure 1 display an example of CRDs with clear counter-rotation between inner and outer stellar disks. Figure 1(c) displays the v_* field, with the black solid and dashed lines representing the photometric major and minor axes. Figure 1(d) displays the v_* along major axis, with the black circles showing v_* as a function of radius. We perform polynomial fitting for these black circles, with the best-fitting result shown as a black curve. On this curve, we find three positions with $v_* = 0$, one at the galaxy center, one on the positive semi-major axis, and another on the negative semi-major axis. These three zero-velocity points (marked by vertical lines) divide the curve into four segments (A/B/C/D), and the directions of velocity in two adjacent segments are opposite. We select 448 candidates satisfying these criteria. We visually inspect these galaxies to delete galaxy pairs within the field-of-view, ongoing mergers, irregular morphology, or disturbed v_* pattern, leaving 45 CRDs exhibiting counter-rotation between inner and outer stellar disks. Thirty-three out of these 45 CRDs show both counter-rotation and 2σ features. Thus our final sample include 147 CRDs, which accounts for 1.5% of the MaNGA survey. The basic physical properties of these galaxies are provided in the table in appendix, and the corresponding kinematic maps can be accessed on Marvin Web¹

¹ <https://magrathea.sdss.org/marvin/>

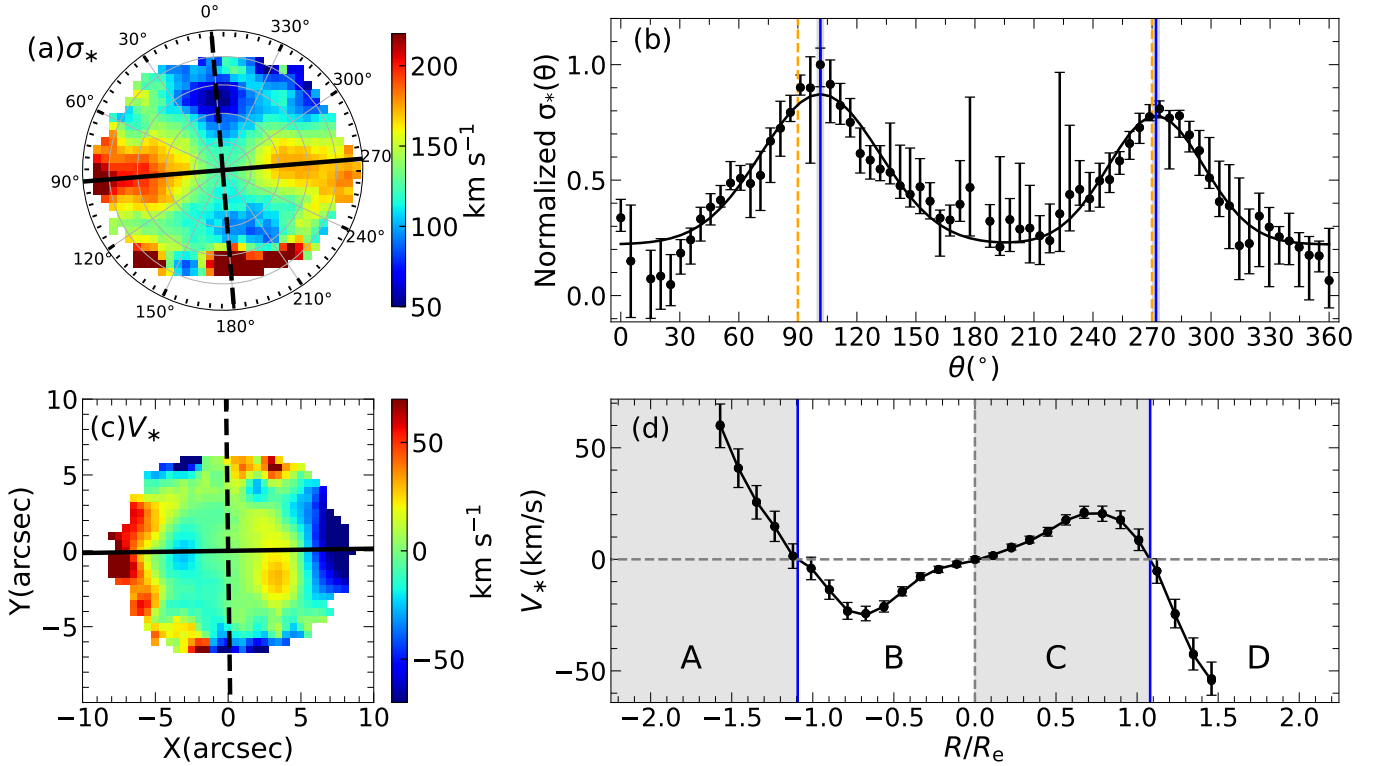


Figure 1. Two examples of our sample selection. (a) The stellar velocity dispersion field in polar coordinate. The black solid and dashed lines show the photometric major and minor axes. (b) Normalized σ_* as a function of θ . The black circle represents the median σ_* in each sector, with the black vertical bar showing the $\pm 1\sigma$ scattering range. The black curve shows the best-fitting double Gaussian model. The vertical blue lines and grey-shaded areas mark the directions of two peaks and corresponding errors. The vertical orange dashed lines mark $\theta = 90^\circ$ and $\theta = 270^\circ$, the photometric major axis. (c) The stellar velocity field. The black solid and dashed lines show the photometric major and minor axes. (d) v_* along major axis. The black circles show the v_* as a function of radius, with the black vertical bar showing the v_* error. The black curve shows the best result of polynomial fitting. The horizontal grey dashed line marks $v_* = 0 \text{ km s}^{-1}$. The vertical grey dashed line marks the radius of central velocity-zero point. The vertical blue solid lines mark the radii of the other two velocity-zero points.

using the MaNGA-ID or Plate-IFU. We cross-match these galaxies with the catalog provided by [Chang et al. \(2015\)](#) to obtain their global stellar mass and star formation rate. These properties were derived from SED fitting using a combination of SDSS and WISE photometry. This process leaves a subset of 138 CRDs for our subsequent analysis.

The CRD sample is classified into six types based on their stellar and gas kinematics. Figure 2 shows six examples of corresponding types. In each panel, the three maps show stellar velocity dispersion field, stellar velocity field, and gas velocity field traced by $\text{H}\alpha$. Figure 2(a) displays an example of 34 CRDs classified as Type NO-EML, in which over 75% spaxels within $1.5 R_e$ have $\text{H}\alpha$ S/N lower than 3, thus we can not get robust gas velocity fields. The black solid line in the stellar velocity dispersion field represents the photometric major axis. In this study, we require median spectral S/N > 3 for reliable stellar properties and emission-line S/N > 3 for reliable gas properties in all the spatially resolved analyses. Figure 2(b) displays an example of eight CRDs classified as Type MIS, in which both stellar disks are misaligned with the gas disk. We use KINEMETRY package ([Krajnović et al. 2006](#)) to fit the position angle for gas disk (Φ_{gas}), and the position angles for inner and outer stellar disks (Φ_*), respectively. Type MIS satisfy the criterion that position angle offsets $\Delta\Phi = |\Phi_* - \Phi_{\text{gas}}| > 30^\circ$ for both inner and outer stellar disks.

The remaining 96 galaxies are classified into four types following the criteria from [Bao et al. \(2022\)](#). Sixty-six of them exhibit 2σ features in their stellar velocity dispersion fields, but lack of evidence for two counter-rotating stellar disks in the stellar velocity fields. This phenomenon occurs because one of the two stellar disks overshines the other, and the brighter disk dominates the stellar rotation. We classify these 66 galaxies into 41 Type CO in which the stellar and gas disks are co-rotating (with position angle offset lower than 30°), and 25 Type CT in which the gas and stellar disks are counter-rotating with each other. Figures 2(c) and 2(d) show examples of Type CO and Type CT, respectively.

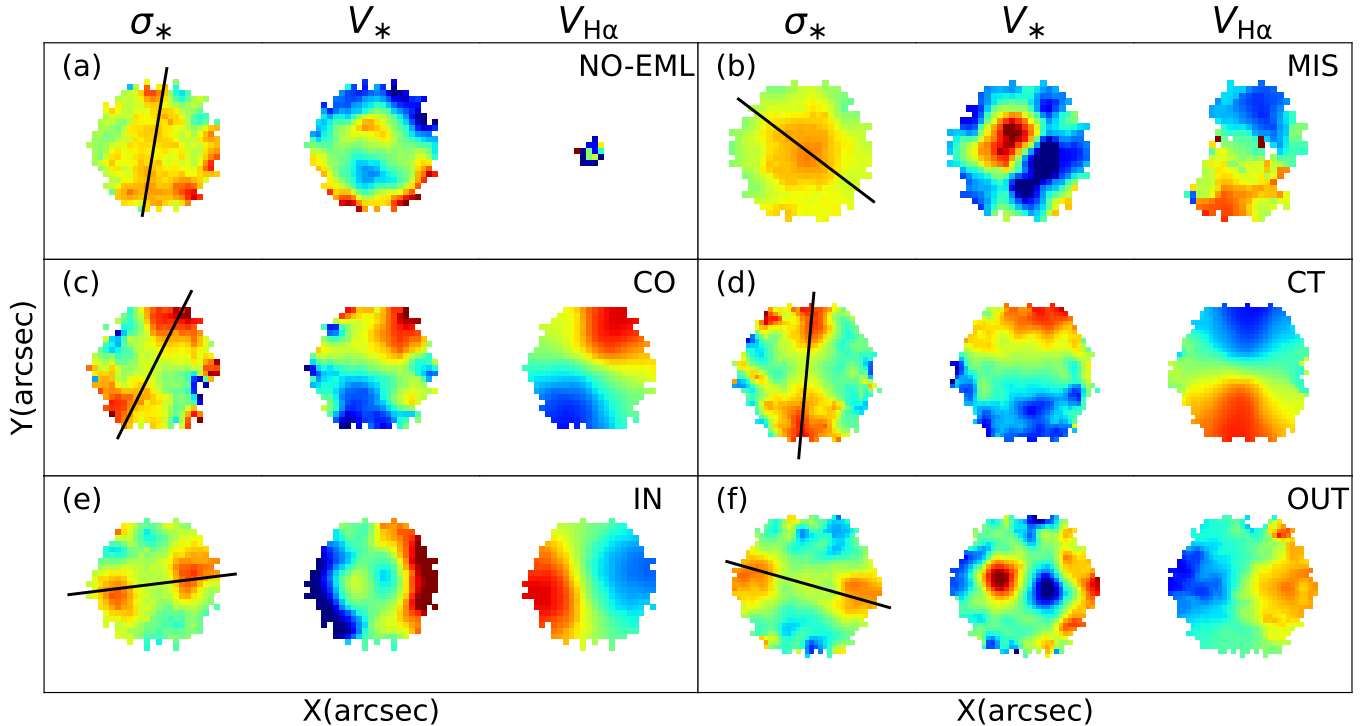


Figure 2. Examples of different types of CRDs. (a) Type NO-EML, where the gas emission can be neglected. (b) Type MIS, where both stellar disks are misaligned with the gas disk. (c) Type CO, where one stellar disk overshines the other, with the brighter stellar disk co-rotating with the gas disk. (d) Type CT, where one stellar disk overshines the other, with the brighter stellar disk counter-rotating with the gas disk. (e) Type IN, where the inner stellar disk is co-rotating with the gas disk. (f) Type OUT, where the outer stellar disk is co-rotating with the gas disk. In all the panels, three subplots sequentially represent stellar velocity dispersion field, stellar velocity field, and gas velocity field traced by $H\alpha$. The black solid line in each stellar velocity dispersion field represents the photometric major axis.

The other $(96 - 66 =) 30$ galaxies clearly show two counter-rotating stellar disks in the stellar velocity fields. We separate these 30 CRDs into 17 Type IN and 13 Type OUT. The gas disk is co-rotating with the inner stellar disk in Type IN (Figure 2e), while it is co-rotating with the outer stellar disk in Type OUT (Figure 2f). Bao et al. (2022) found that these four types have different stellar population age, with Type CO and Type IN being relatively younger. Type CO and Type IN are dominated by SF galaxies with abundant pre-existing gas. The effective interaction between pre-existing and accreted gas can trigger active star formation, resulting in younger stellar population age. Meanwhile, Type CT and Type OUT are primarily QS galaxies with lower amount of pre-existing gas. For the following analysis, we combine Type CO and Type IN together as Type CO+IN, and Type CT and Type OUT as Type CT+OUT.

To understand the formation mechanisms for CRDs, we build a control sample without any counter-rotation between gas and/or stellar components for comparison. Three control galaxies are closely matched to each CRDs in two dimensional parameter space of global stellar mass ($|\Delta \log M_*| < 0.1$) and star formation rate ($|\Delta \log \text{SFR}| < 0.2$). Figure 3(a) displays the distributions of galaxies in the $\log M_* - \log \text{SFR}$ plane. The grey contour represents the galaxies with robust global stellar mass and SFR measurements in the catalog of Chang et al. (2015). The black dashed line separates these galaxies into star-forming (SF) and quiescent (QS) sequence. The blue, green, red and black circles represent Type CO+IN, Type CT+OUT, Type MIS and Type NO-EML, respectively. The grey squares represent the control sample. Table 1 lists the numbers and fractions of SF galaxies for different types of CRDs. The first column lists the type names, followed by the total number of galaxies for each type in the second column. The third and fourth columns provide the numbers of SF galaxies and their fractions in the relevant types of CRDs. It turns out that Type CO+IN are dominated by SF galaxies, whereas Type CT+OUT, Type NO-EML and Type MIS are dominated by QS galaxies. The SF fraction declines from 67.2% in Type CO+IN to 17.6% in Type NO-EML.

Figures 3(b) and 3(c) display the $\log M_*$ and $\log \text{SFR}$ distributions for different types of CRDs, with blue, green, red and black histograms representing Type CO+IN, Type CT+OUT, Type MIS and Type NO-EML, respectively.

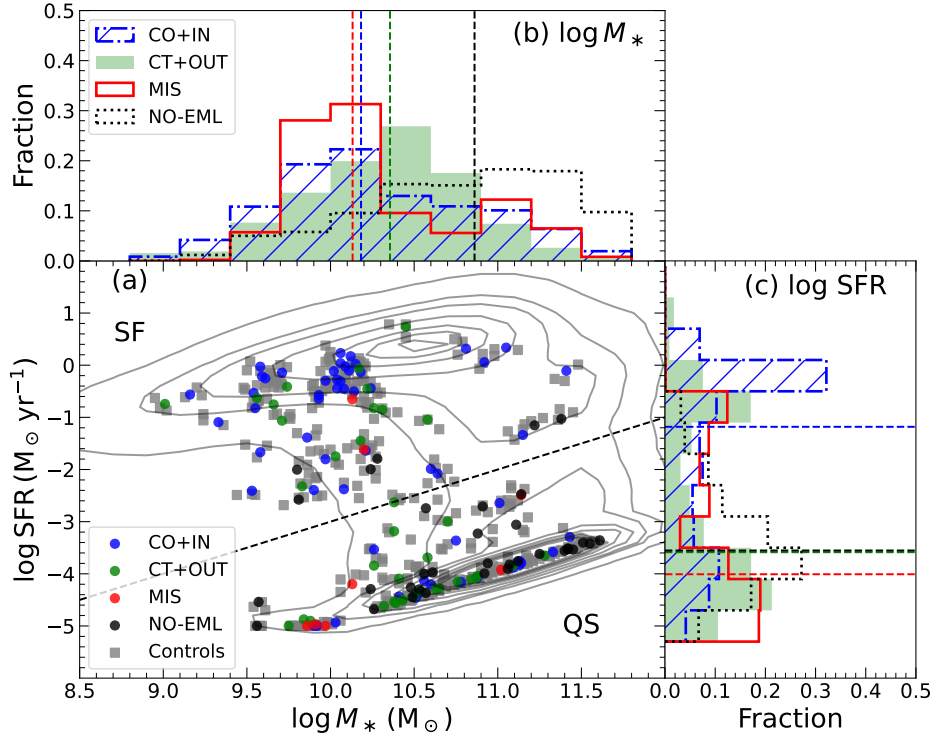


Figure 3. Distribution of CRD sample in the $\log M_{*}$ - $\log \text{SFR}$ plane. (a) The grey contour shows the distribution of SDSS spectroscopic galaxy sample from Chang et al. (2015) catalog. The blue, green, red and black circles show the distributions of Type CO+IN, Type CT+OUT, Type MIS and Type NO-EML, respectively. The black dashed line classifies galaxies into SF and QS sequence. (b) Distribution of stellar mass. (c) Distribution of star formation rate. In panels (b) and (c), the blue, green, red and black histograms show the M_{*} and SFR distributions of Type CO+IN, Type CT+OUT, Type MIS and Type NO-EML, respectively. The blue, green, red and black vertical lines show the corresponding median values.

Table 1. The numbers and fractions of SF galaxies for different types of CRDs.

Type of CRDs	Total number	Number of SF galaxies	Fraction of SF galaxies
Type CO+IN	58	39	67.2%
Type CT+OUT	38	14	36.8%
Type MIS	8	2	25.0%
Type NO-EML	34	6	17.6%

The blue, green, red and black vertical (or horizontal) lines show the median values of $\log M_{*}$ (or $\log \text{SFR}$) for corresponding distributions. In Figure 3(b), Type NO-EML exhibit the highest stellar mass with a median value of $\log(M_{*}/M_{\odot}) \sim 10.9$, while Type CT+OUT are about 0.5 dex lower. Type CO+IN and Type MIS show comparable stellar mass, both having the lowest median values of $\log(M_{*}/M_{\odot}) \sim 10.2$. In Figure 3(c), Type CO+IN display the highest star formation rate with a median value of $\log(\text{SFR}/M_{\odot} \text{ yr}^{-1}) \sim -1.2$. The star formation rate of Type CT+OUT and Type MIS is 2.4 dex lower than that of Type CO+IN. Although Type MIS have stellar mass comparable to Type CO+IN, it exhibits the lowest star formation rate of $\log(\text{SFR}/M_{\odot} \text{ yr}^{-1}) \sim -4.0$.

3. RESULTS

3.1. Global properties

We compare the global properties between the CRD sample and their control sample, including galaxy morphology traced by bulge-to-total ratio, molecular gas content scaled from Balmer decrement, and galaxy environment indicated by neighbour number and tidal strength parameter. Under the assumption of gas accretion formation mechanism, the

interaction between pre-existing and accreted gas can redistribute angular momentum and trigger gas inflows. We are interested in: (1) the impact of gas accretion on galaxy evolution, (2) how it modulates the molecular gas content, and (3) whether CRDs prefer to reside in certain environments.

3.1.1. Morphology

Figure 4 compares the distributions of bulge-to-total ratio between Type CO+IN (panel a), Type CT+OUT (panel b), Type NO-EML (panel c), Type MIS (panel d) and their control samples. In each panel, the colored histogram represents the CRD sample, while the gray histogram represents the control sample. The vertical lines indicate the median values of corresponding distributions.

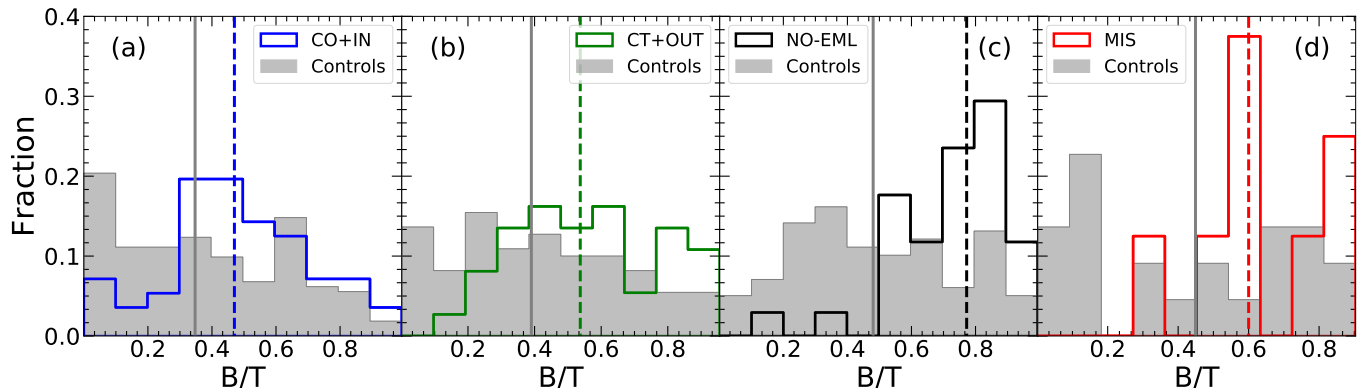


Figure 4. The distributions of bulge-to-total ratio. Four panels sequentially display the B/T distributions for Type CO+IN, Type CT+OUT, Type NO-EML, Type MIS and their control samples. The colorful histograms show the B/T distributions for different CRD types. The grey histograms show the B/T distributions for their control samples. The colorful and grey vertical lines show the corresponding median values.

All the CRD types in Figure 4 show larger bulge-to-total ratios than their control samples, indicating the more bulge-dominated morphology of these CRDs. In the four panels, the median B/T of the control samples are below 0.5, suggesting that the bulge tend to contribute less than half of the total light in these galaxies. However, except for Type CO+IN whose median B/T value is slightly below 0.5 (~ 0.47), the median B/T of Type CT+OUT (~ 0.54), Type NO-EML (~ 0.77), and Type MIS (~ 0.60) all exceed 0.5. These CRDs are believed to form mainly by accreting external gas. As suggested by Chen et al. (2016), AM redistribution occurs during interactions between pre-existing and accreted gas, driving gas inflows and central star formation. This enhanced star formation in the center then contributes to the growth of bulge, and alters the system’s light distribution.

3.1.2. Gas content

Current studies suggest that CRDs accrete gas from external environments, which may result in elevated gas masses. Conversely, interactions between pre-existing and accreted gas can drive AM redistribution and gas inflows, leading to rapid gas-to-star transformation. These two competing processes jointly modulate the gas content in CRDs. The molecular gas surface density (Σ_{mol}) is estimated as $\Sigma_{\text{mol}} \sim 23 M_{\odot} \text{ pc}^{-2} A_V$, where A_V is V-band extinction calculated from the Balmer decrement (Barrera-Ballesteros et al. 2020). The Balmer decrement is defined as the flux ratio of $H\alpha$ to $H\beta$ Balmer lines ($H\alpha/H\beta$). The fluxes of $H\alpha$ and $H\beta$ are obtained from the MaNGA DAP, which are derived through Gaussian profile fitting using pPXF. The total molecular gas mass (M_{mol}) is obtained as $\sum_i (S_{\text{spaxel}}^i \times \Sigma_{\text{mol}}^i)$, where S_{spaxel}^i is the physical area and i means the i -th spaxel.

Figure 5 displays the distributions of molecular gas mass fraction defined as $\log(M_{\text{mol}}/M_*)$ between CRDs and control samples, with colors coded in the same way as Figure 4. It is clearly shown in Figure 5 that all the three types of CRDs have lower molecular gas mass fraction than their control samples. The median value of molecular gas mass fraction of Type CO+IN is ~ 0.5 dex lower than their control sample in Figure 5(a). The difference between Type CT+OUT and their control sample increases to ~ 1.1 dex in Figure 5(b). And the difference between Type MIS and their control sample is ~ 0.6 dex, which falls between those of the other two types.

Similar results are reported in the gas-star misaligned samples selected from MaNGA survey (Duckworth et al. 2020; Zhou et al. 2022) as well as that from IllustrisTNG simulation (Lu et al. 2021). The lower molecular gas mass fraction

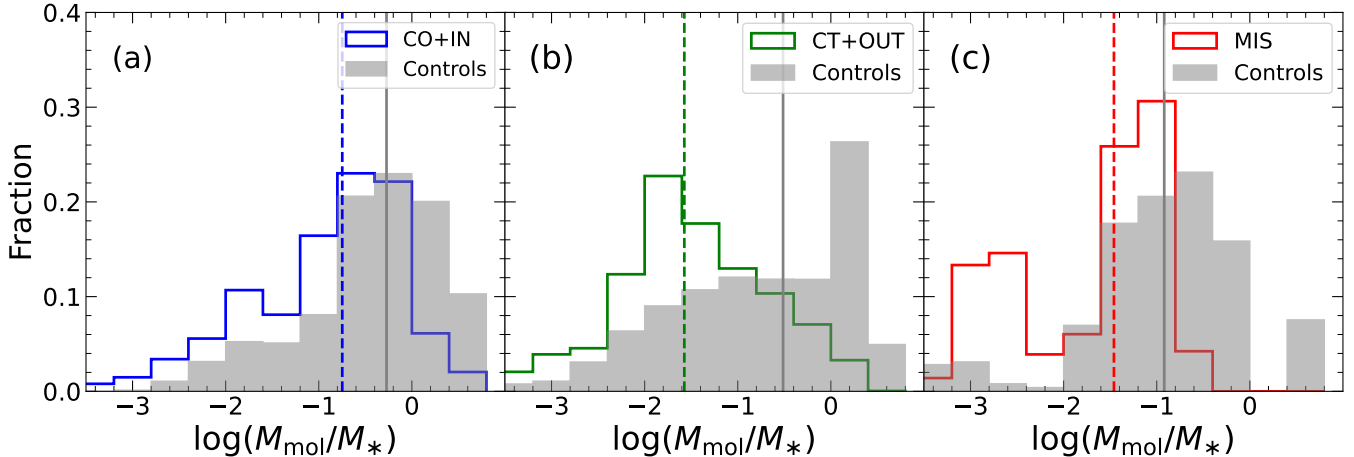


Figure 5. The distributions of molecular gas mass fraction. Three panels sequentially display the $\log(M_{\text{mol}}/M_*)$ distributions for Type CO+IN, Type CT+OUT, Type MIS and their control samples. The colorful histograms show the $\log(M_{\text{mol}}/M_*)$ distributions for different CRD types. The grey histograms show the $\log(M_{\text{mol}}/M_*)$ distributions for their control samples. The colorful and grey vertical lines show the corresponding median values.

could naturally result from efficient consumption. Molecular gas, the raw material for star formation, is efficiently consumed by the enhanced star formation in these galaxies, which is triggered by the interaction between pre-existing and accreted gas.

3.1.3. Large-scale environment

In the mechanism of external gas accretion, the external gas primarily resides outside the virial radius of the dark-matter halo that hosts the galaxy, and by accretion over cosmic time it becomes part of the baryon pool that supplies the evolution of this galaxy (Sánchez et al. 2012). The origin of external gas involves sources such as the intergalactic medium (IGM; Cao & Pan 2025), satellites (Liu & Lan 2026), and cosmic web (Bao et al. 2025). Under such a mechanism – the formation of CRDs occurs primarily through the external gas accretion – we would expect these galaxies to reside predominantly in sparse environments conducive to gas accretion. Conversely, in dense environments, mechanisms such as gas stripping or halo heating may suppress this process.

Based on the ATLAS^{3D} survey, Davis et al. (2011) demonstrated that early-type galaxies in dense groups and clusters are more likely to exhibit kinematic alignment between gas and stars, whereas misalignments tend to dominate in field galaxies. Focusing on 66 gas-star misaligned galaxies with diverse star formation types selected from the early data release of the MaNGA survey, Jin et al. (2016) further showed that these systems all reside in relatively isolated environments. With a sample size about ten times larger, Zhou et al. (2022) revisited the environmental dependence of misaligned galaxies and corroborated this result. Here, we compare the environmental parameters (the neighbour number and the tidal strength parameter) between our CRDs and their control samples.

The neighbour number (N_{neigh}) is defined as the number of neighbours with r -band absolute magnitude brighter than -19.5 within 500 km s^{-1} line-of-sight velocity and 1 Mpc projected distance in a volume-limited sample with $z < 0.15$ (Argudo-Fernández et al. 2015). The tidal strength parameter Q_{ISS} is a description of the total gravitational interaction strength by all the neighbours within this limited volume. The estimation method is described in Argudo-Fernández et al. (2015), and the result is released in the Galaxy Environment for MaNGA Value Added Catalog (GEMA-VAC)². It is defined as

$$Q_{\text{ISS}} = \log\left[\sum \frac{M_i}{M_t} \left(\frac{D_t}{d_i}\right)^3\right], \quad (1)$$

where M_t and M_i are the stellar mass of the primary galaxy and its i -th neighbor, d_i is the projected distance between the primary galaxy and the i -th neighbor, and D_t is the diameter of the primary galaxy.

² https://data.sdss.org/datamodel/files/MANGA_GEMA/GEMA_VER/GEMA.html

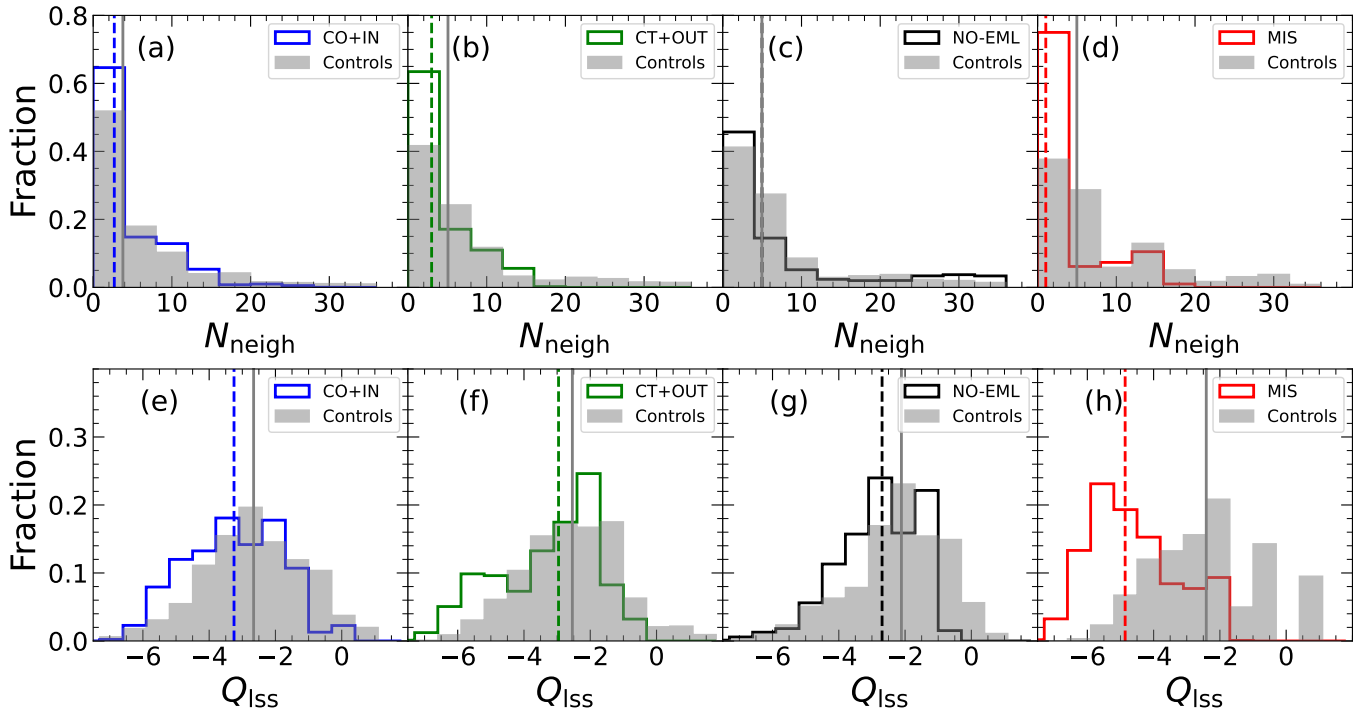


Figure 6. The distributions of environmental parameters. The top and bottom rows display the distributions of neighbour number and tidal strength parameter, respectively. Four panels in each row sequentially display the distributions for Type CO+IN, Type CT+OUT, Type NO-EML, Type MIS and their control samples. The colorful histograms show the distributions for different CRD types. The grey histograms show the distributions for their control samples. The colorful and grey vertical lines show the corresponding median values.

Figure 6 displays the distributions of N_{neigh} in the top panels and $Q_{1\text{ss}}$ in the bottom panels, with colors coded in the same way as Figure 4. From left to right, the CRD types are illustrated Type CO+IN, Type CT+OUT, Type NO-EML and Type MIS. The two vertical lines in each panel mark the median values of corresponding distributions. All these types of CRDs tend to reside in more isolated environments with lower values of $Q_{1\text{ss}}$ than their control samples. Similar trends are also found in N_{neigh} for Type CO+IN, Type CT+OUT and Type MIS, but with less significance. Figures 6(d) and 6(h) show the largest difference between Type MIS and their control of all the CRD types. Type MIS host two counter-rotating stellar disks, with both stellar disks rotating in directions inconsistent with the gas disk. This configuration suggests that such galaxies have experienced multiple episodes of external gas accretion. Given the complexity of their formation processes, we will conduct a detailed investigation of these galaxies in future work.

3.2. Spatially resolved properties

In this section, we study the spatially resolved properties of the CRD sample, including gas-phase metallicity, stellar population age traced by 4000 Å break and light-weighted stellar metallicity. The dilution of gas-phase metallicity can serve as evidence of CRDs accreting gas from the external environments. Meanwhile, combining the stellar population age and light-weighted stellar metallicity, we can understand the star formation and metal enrichment cycle under the influence of gas accretion.

3.2.1. Gas-phase metallicity

Gas-phase metallicity is one of the most fundamental physical properties of galaxies, reflecting both the amount of gas reprocessed by stellar nucleosynthesis and the exchange of gas between galaxies and surrounding environments. CRDs are widely regarded as key tracers of evolution dominated by external processes. External mechanisms – such as minor/major mergers or gas accretion – can bring in gas with metallicity distinct from the pre-existing gas within galaxies. By comparing the gas-phase metallicity of CRDs with that of their control samples, we can gain critical insights into the origin of the external gas and elucidate how gas accretion processes shape galaxy evolution.

Strong-line abundance diagnostics, developed based on stellar population synthesis and photoionization models, are primarily applicable to HII regions (Kewley & Dopita 2002). However, in most spaxels of QS galaxies, the gas is not excited by star formation. Following Jin et al. (2016), we therefore adopt the $N2S2 = \log([\text{N II}]\lambda 6583/([\text{S II}]\lambda 6717 + [\text{S II}]\lambda 6731))$ as an alternative gas-phase metallicity indicator. Dopita et al. (2016) and Kashino et al. (2016) proposed that this ratio serves as a proxy for the N/O ratio and exhibits a tight correlation with O/H abundance at $12 + \log(\text{O}/\text{H}) > 8.0$. Additionally, the two emission lines are closely spaced in wavelength, making dust extinction corrections negligible. The gas-phase metallicity is calculated following the scaling relation from Smirnova-Pinchukova et al. (2022): $12 + \log(\text{O}/\text{H}) = 8.875 + 0.827 \times N2S2 - 0.288 \times N2S2^2$.

Figure 7 compares the radial gradients of gas-phase metallicity between Type CO+IN (panel a), Type CT+OUT (panel b), Type MIS (panel c) and their control samples, respectively. In Figure 7, the colored circles represent the median metallicity within each radial bin for CRD samples, with the error bars showing 40% - 60% scattering ranges. The error bar reflects the scatter in metallicity among the sample (or control) galaxies in each radial bin, with a typical value of ~ 0.04 dex. Using the flux errors of the emission lines provided by the MaNGA DAP, we also estimated the metallicity measurement error for each spaxel via error propagation. The typical measurement error in each radial bin is ~ 0.03 dex, which is smaller than the typical scatter in metallicity (~ 0.04 dex). The gray squares and error bars represent the median metallicity and scattering ranges for control samples. As shown in Figure 7(a), Type CO+IN exhibit ~ 0.04 dex higher gas-phase metallicity than their control sample at all radii. In contrast, Type CT+OUT show ~ 0.07 dex lower gas-phase metallicity than the control sample in Figure 7(b). Meanwhile, Type MIS in Figure 7(c) exhibit ~ 0.07 dex lower gas-phase metallicity than their control sample.

The observed gas-phase metallicity is the result of competition between the enrichment of stellar nucleosynthesis and the dilution of metallicity by accreting low-metallicity external gas. Considering that Type CO+IN are dominated by SF galaxies, the ~ 0.04 dex higher gas-phase metallicity in these galaxies compared to their controls can be attributed to enrichment from ongoing star formation. In the closed-box model (Dalcanton 2007), metallicity primarily depends on the gas mass fraction $f_{\text{gas}} \equiv M_{\text{gas}}/(M_{\text{gas}} + M_{\star})$; thus, abundances rise rapidly as a substantial fraction of the available gas is converted into stars. The ~ 0.07 dex lower gas metallicity in Type CT+OUT compared to their control sample indicates that metallicity dilution through external gas accretion is more effective than enrichment process. The misalignment between the gas disk and two stellar disks in Type MIS suggests that the gas component is newly accreted after both stellar disks have formed. Stellar nucleosynthesis-induced metallicity enrichment can be neglected. The ~ 0.07 dex lower gas-phase metallicity in Type MIS compared to their control sample is primarily attributed to dilution from gas accretion.

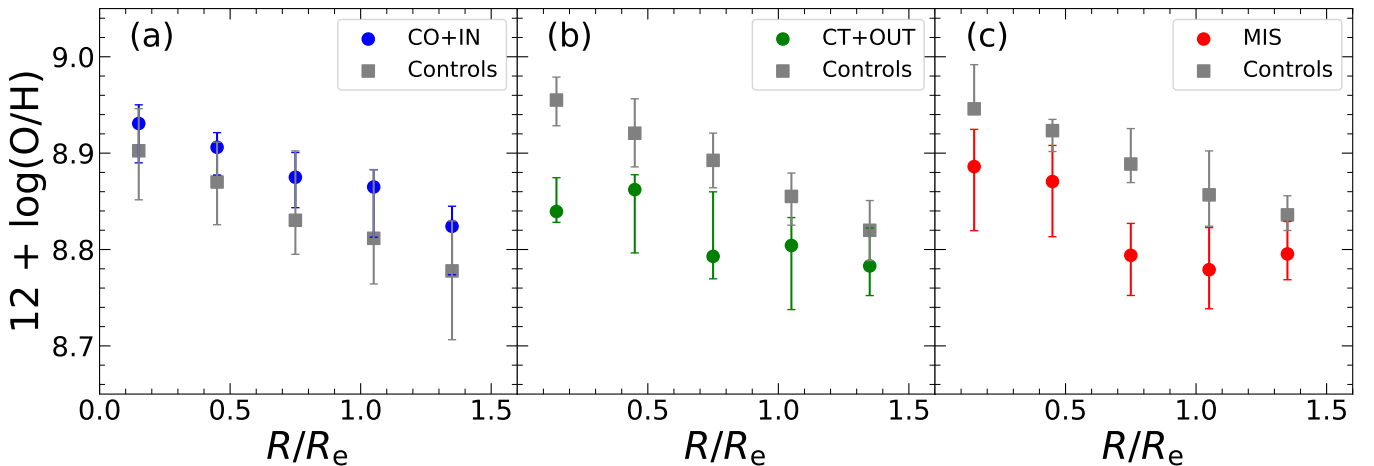


Figure 7. The radial gradients of gas-phase metallicity. Three panels sequentially display the gas-phase metallicity radial gradients for Type CO+IN, Type CT+OUT, Type MIS and their control samples. The colorful circles show the median gas-phase metallicity for different CRD types. The grey squares show the median gas-phase metallicity for their control samples. The colorful and grey error bars show 40%-60% scattering ranges for corresponding radial gradients.

3.2.2. Stellar population properties

Figure 8 displays the radial gradients of D_n4000 (left) and light-weighted stellar metallicity (right). In each panel, the blue, green, red and black circles represent the median values for Type CO+IN, Type CT+OUT, Type MIS and Type NO-EML. The corresponding error bars show the 40% - 60% scattering ranges, following the same representation as in Figure 7. In Figure 8(a), stellar populations become older following a sequence of Type CO+IN, Type CT+OUT, Type MIS, and Type NO-EML at all radii. This trend aligns with the result in Table 1, where the types of CRDs with higher fractions of SF galaxies tend to host younger stellar populations. Type CO+IN are dominated by SF galaxies with abundant pre-existing gas, the effective interaction between pre-existing and accreted gas can trigger active star formation. Meanwhile, Type CT+OUT are dominated by QS galaxies with lower amount of pre-existing gas. This results in lower angular momentum lose efficiency through gas interaction and thus suppressing star formation activity. Type NO-EML, which possess the highest stellar mass, oldest stellar populations, and largest fraction of QS galaxies among all the types of CRDs, may represent the final evolutionary stage of the other types. About Type MIS, we will discuss them in Section 4.1 in more detail.

Figure 8(b) illustrates that the light-weighted stellar metallicity increases consistently with the sequence traced by D_n4000 . By combining the trends observed in both panels, we conclude that CRDs with older stellar populations exhibit higher stellar metallicity. The higher stellar metallicity in older galaxies fundamentally arises from the process of successive generations of star formation and the metal enrichment cycle – older galaxies have experienced longer duration of star formation, where each generation of stars injects heavy elements into the interstellar medium through nucleosynthesis and feedback. Subsequent star formation then utilizes these metal-enriched gas, leading to a gradual increase in stellar metallicity over time.

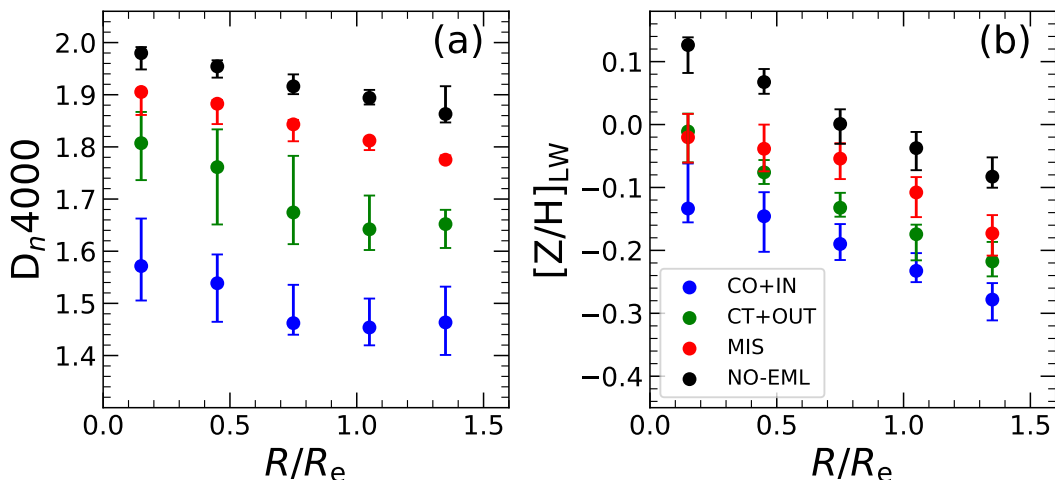


Figure 8. The radial gradients of stellar population properties for different types of CRDs. (a) The D_n4000 radial gradients. (b) The $[Z/H]_{LW}$ radial gradients. In each panel, the blue, green, red and black circles show the median radial gradients for Type CO+IN, Type CT+OUT, Type MIS and Type NO-EML, respectively.

4. DISCUSSION

4.1. Multiple gas accretion events in nearby galaxies

In this section, we focus on eight CRDs classified as Type MIS, which host two counter-rotating stellar disks and exhibit misalignment between both stellar disks and the gas disk. We propose that these galaxies underwent multiple gas accretion events with differing AM directions. So far, observations of multiply misaligned galaxies remain rare (Cao et al. 2022), while these galaxies are crucial for understanding how the frequent accretion events contribute to galaxy assembly.

Globally, Type MIS exhibit the lowest stellar mass with $\log(M_*/M_\odot) \sim 10.2$ and star formation rate with $\log(\text{SFR}/M_\odot \text{ yr}^{-1}) \sim -4.0$ among all the types of CRDs. Additionally, they show distinct properties compared to their control sample: they have high bulge-to-total ratio with $B/T \sim 0.60$, low molecular gas mass fraction with $\log(M_{\text{mol}}/M_*) \sim -1.5$, and reside in least dense environments with $Q_{\text{LSS}} \sim -4.9$ compared to the other types of CRDs

and control samples (Figure 6). Spatially resolved properties further reveal that Type MIS display ~ 0.07 dex lower gas-phase metallicity than the control sample at all radii (Figure 7c) and host the second-oldest stellar populations with $D_n4000 \sim 1.8$ among all the types of CRDs (Figure 8a).

The significantly less dense environments of Type MIS reduce the impacts of ram pressure stripping and halo heating, facilitating more frequent gas accretion events. Early gas accretion supplied the formation of a counter-rotating stellar disk relative to the pre-existing one. The currently observed gas disk originates from a recent accretion episode, which is independent of the early gas accretion event. The older stellar populations in Type MIS compared to Type CO+IN and Type CT+OUT may be attributed to the earlier formation of their counter-rotating stellar disks. The lower molecular gas content in Type MIS may be attributed to selection bias: early star formation efficiently depleted the gas reservoir, making these galaxies more likely to be classified as Type MIS. This arises because the negligible interaction between recently accreted gas and pre-existing gas minimizes the impact of gas mixing, preserving the AM of the recently accreted gas. Consequently, the primary effect of this recent accretion episode is gas dilution, leading to the lower gas-phase metallicity observed in Type MIS compared to control sample.

Cao et al. (2022) identified galaxies with misaligned gas disks from the MaNGA survey, where two gas disks are also misaligned with the stellar disk. However, owing to the large collision cross-sections of gas components – which result in short dynamical friction timescales (~ 100 million years) – only two such galaxies were confirmed. In this work, eight CRDs classified as Type MIS significantly expand the observational sample of nearby galaxies that have undergone multiple gas accretion events. Their existence demonstrates that frequent gas accretion plays a critical role in galaxy assembly, even for low-redshift galaxies, they can accrete gas multiple times from their environments. In future work, we will investigate the formation scenario for Type MIS through numerical simulations to gain deeper theoretical insights.

4.2. Formation scenarios for counter-rotating stellar disks

Previous studies have established that external gas accretion is the primary formation mechanism for CRDs. The disk formed from accreted gas inherits the AM of the accreted material and counter-rotates relative to the pre-existing stellar disk. Consequently, in all previous case studies of CRDs, gas disk has been observed to co-rotate with younger stellar disk. Meanwhile, Bevacqua et al. (2022) identified two peculiar CRDs in the MaNGA survey, where gas disk co-rotates with older stellar disk. They proposed that these galaxies formed via the merger of a disk galaxy and a gas-poor galaxy hosting younger stellar populations in a retrograde orbit.

Analyzing the gas and stellar velocity fields, along with D_n4000 maps, of our CRD sample, we identify four peculiar CRDs where gas disk co-rotates with older stellar disk. Figure 9 presents an example of such galaxies. We further examine their DESI g, r, z composite images (Figure 9a showing an example), which are two magnitudes deeper than SDSS observations. However, following the method of Li et al. (2021), we detect no merger remnant or interaction feature with companion in these images.

Figures 9(b), 9(c) and 9(d) present the spatially resolved D_n4000 map alongside the gas and stellar velocity fields for the example. Two key features are evident: (1) the inner and outer stellar disks counter-rotate, with the outer stellar disk co-rotating with the gas disk; (2) the outer stellar disk hosts older stellar populations with higher D_n4000 . We propose an alternative formation scenario for these peculiar CRDs involving external gas accretion. Initially, the older stellar disk formed from pre-existing gas. Subsequent external gas accretion supplied counter-rotating gas to these galaxies. The interaction between the pre-existing and accreted gas redistributes the angular momentum, which further triggers gas inflows and the formation of inner stellar disk. Hence, the inner stellar disk is counter-rotating with the outer one, and hosts relatively younger stellar populations. Since the pre-existing gas has higher AM than the accreted gas, it governs the rotation of the gas disk, resulting in co-rotation between the gas disk and the outer stellar disk, which hosts relatively older stellar populations.

The stellar velocity field shown in Figure 9(c) reveals extremely low rotational velocities in the inner stellar disk, with absolute values below 10 km s^{-1} . This suggests that our selection criteria may have overlooked CRDs featuring slowly rotating inner stellar disk, indicating that the 1.5% CRD detection rate should be considered as a lower limit for the incidence rate for CRDs in the MaNGA survey. Pan et al. (2014) investigated nearby green-valley galaxies, and detected blue-core in 63% of the early-type green-valley galaxies, suggesting that gas inflows can fuel star formation in their center. Chen et al. (2019) constructed a sample of blue-core galaxies from the MaNGA survey, and found that 26% of these galaxies exhibit misalignment between gas and stellar components, indicating external gas accretion. These blue-core galaxies with younger stellar populations in the center may have undergone a formation scenario

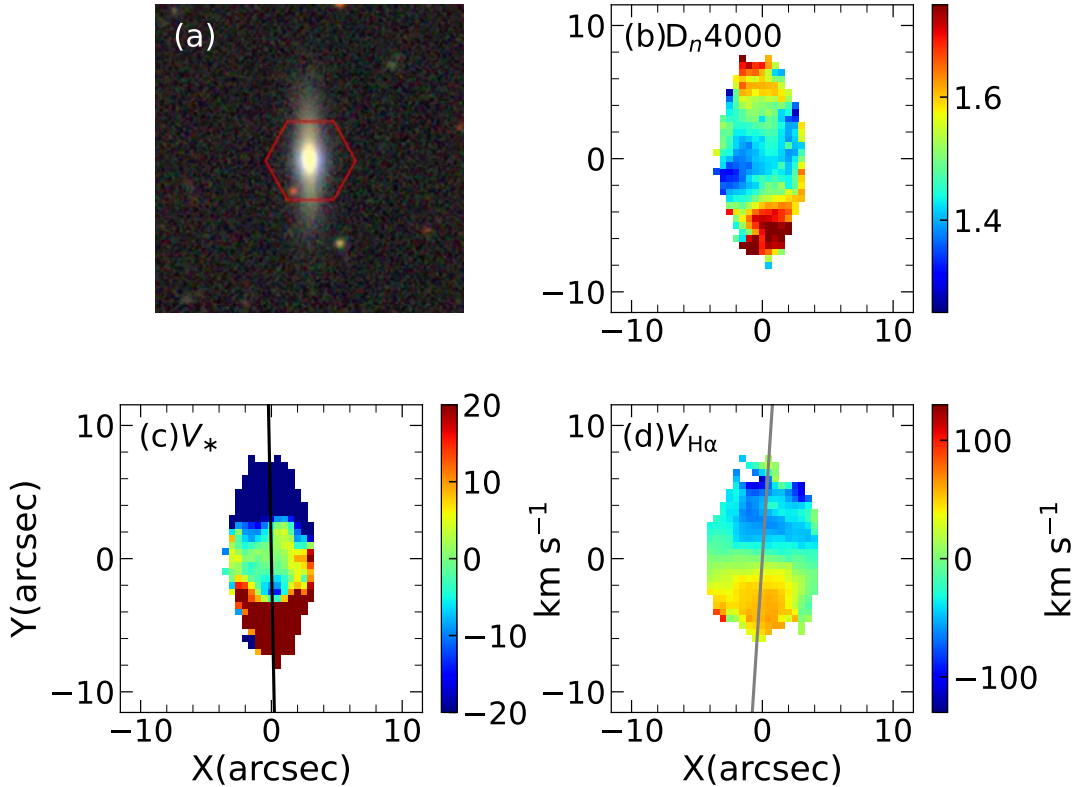


Figure 9. An example for the peculiar CRDs, where the gas disk co-rotates with the older stellar disk. (a) DESI g, r, z composite image. (b) D_n4000 map. Red color shows the relatively older stellar populations, and blue color shows the younger stellar populations. (c) Stellar velocity field. The black solid line shows the kinematic position angle of outer stellar disk. (d) The gas velocity field traced by $H\alpha$. The grey solid line shows the kinematic position angle of gas disk.

similar to the CRDs in Figure 9. Their exclusion from the CRD sample can be attributed to the exceptionally low rotational velocities in the inner stellar disk.

5. CONCLUSION

In this study, we construct a sample of 147 galaxies with counter-rotating stellar disks from the MaNGA survey, and 138 out of them have global M_* and SFR measurements from the catalog of Chang et al. (2015). We classify these 138 CRDs into six distinct types, compare global and spatially resolved properties between CRDs and their control samples with similar stellar mass and star formation rate. The main results are as follows:

1. All the types of CRDs exhibit more prominently bulge-dominated morphologies, lower molecular gas mass fraction, and reside in less dense environments compared to their control samples. These features support a mechanism that the formation of CRDs is dominated by external gas accretion.
2. Type CO+IN are dominated by star-forming galaxies with abundant pre-existing gas in their progenitors. The interaction between pre-existing and accreted gas triggers active star formation, resulting in the youngest stellar populations among all the types of CRDs. In contrast, Type CT+OUT are dominated by quiescent galaxies, hosting older stellar populations than Type CO+IN. Among all the types of CRDs, Type NO-EML have the oldest stellar populations and highest stellar mass, suggesting that they may represent the final evolutionary stage of the other types.
3. For Type MIS, the fact that both stellar disks are misaligned with the gas disk implies that their formation is governed by multiple gas accretion events with differing AM direction of the accreted gas. We propose that early gas accretion triggered the formation of a counter-rotating stellar disk relative to the pre-existing one, while the recently accreted gas governs the rotation of the gas disk.

4. We identify four CRDs where the gas disk co-rotates with the older stellar disk. [Bevacqua et al. \(2022\)](#) suggested galaxy merger as a formation mechanism. However, we find no evidence of merger remnant or interaction feature with companion in the DESI images of these galaxies. In addition to the galaxy merger, we propose another possible mechanism through external gas accretion, where the pre-existing gas has higher AM than the accreted gas, therefore governing the gas disk's rotation.

APPENDIX

Table 2. Galaxies with counter-rotating stellar disks in MaNGA survey.

MaNGA-ID	Plate	IFU	R.A.	Dec.	z	$\log M_*$ (M_\odot)	$\log \text{SFR}$ ($M_\odot \text{ yr}^{-1}$)	Class
(1)	(2)	(3)	(4)	(5)	(6)	(7)	(8)	(9)
1-109056	8077	6103	39.447	0.405	0.047	10.600	-1.988	Type CO
1-39396	8091	6102	12.291	14.644	0.040	9.970	-0.298	Type CO
1-44183	8138	3704	118.020	44.161	0.026	9.930	-0.643	Type CO
1-37494	8154	3703	44.625	0.794	0.043	10.260	-3.533	Type CO
1-37155	8154	6103	44.349	-0.309	0.029	11.010	-2.643	Type CO
1-52701	8158	6102	61.406	-5.315	0.033	10.750	-3.363	Type CO
1-72795	8240	3701	124.736	44.320	0.117	11.410	-0.108	Type CO
1-277289	8255	3704	165.275	45.293	0.037	9.860	-1.388	Type CO
1-516580	8310	1902	180.255	23.725	0.030	9.610	-0.253	Type CO
1-259068	8341	6102	190.353	45.046	0.025	10.060	0.232	Type CO
1-260458	8447	9101	206.070	39.509	0.062	11.090	-3.883	Type CO
1-260823	8447	3703	208.292	40.119	0.051	10.640	-2.078	Type CO
1-274545	8455	3704	157.686	40.057	0.023	9.590	-0.213	Type CO
1-134361	8487	1902	240.224	47.197	0.046	10.520	-4.398	Type CO
1-210962	8550	12701	246.359	39.871	0.029	11.150	-1.338	Type CO
1-134737	8600	3701	245.912	41.834	0.027	9.580	-1.668	Type CO
1-25632	8611	9101	260.674	59.852	0.027	10.600	-4.203	Type CO
1-546819	8614	3703	257.001	36.344	0.036	11.130	-3.753	Type CO
1-24279	8626	6102	263.173	56.117	0.063	11.330	-3.583	Type CO
1-44312	8718	1902	119.638	45.329	0.022	9.330	-1.093	Type CO
1-45520	8725	3701	125.274	45.848	0.038	9.580	-0.028	Type CO
1-457547	8982	1902	201.921	26.062	0.024	9.970	-1.803	Type CO
1-148987	8999	6102	164.552	50.213	0.024	10.410	-4.438	Type CO
1-323886	9027	3702	245.142	32.935	0.041	10.040	-0.278	Type CO
1-323764	9027	3703	246.054	31.876	0.021	9.550	-0.823	Type CO
1-42660	9195	3704	28.185	13.193	0.026	10.240	-0.443	Type CO
1-121837	9485	3702	120.076	37.609	0.042	10.210	-1.638	Type CO
1-121871	9485	3703	120.767	36.264	0.044	10.140	-0.503	Type CO
1-386322	9506	3703	134.214	27.270	0.019	10.030	-4.933	Type CO
1-537081	9882	3702	206.949	23.367	0.084	11.050	0.337	Type CO
1-317315	9888	1902	238.028	27.559	0.072	11.140	-3.793	Type CO
1-456645	11009	12703	195.775	26.531	0.019	9.930	-0.573	Type CO
1-245176	11013	1902	209.898	55.593	0.041	10.180	-0.133	Type CO
1-78294	11753	6104	147.068	3.906	0.024	10.120	0.172	Type CO
1-407465	11826	6104	190.001	36.872	0.065	10.810	0.317	Type CO
1-234243	11830	3702	197.696	50.093	0.031	10.920	0.057	Type CO
1-1243	11836	1902	150.717	0.069	0.032	10.080	-2.378	Type CO

1-135767	11946	12703	250.229	37.904	0.031	10.560	-4.138	Type CO
1-139814	12489	3703	179.348	4.543	0.020	10.040	-0.443	Type CO
1-2880	12518	3704	159.894	-0.253	0.019	9.160	-0.563	Type CO
1-97176	12679	3701	318.291	-7.632	0.028	10.510	-4.458	Type CO
1-145913	8149	1901	120.222	28.130	0.017	9.900	-4.998	Type IN
1-137890	8249	1901	137.219	44.932	0.027	10.060	0.037	Type IN
1-255220	8253	1902	157.846	42.277	0.022	9.920	-4.998	Type IN
1-274440	8455	1902	155.709	39.369	0.026	9.540	-0.533	Type IN
1-634718	8610	3704	259.630	60.586	0.013	9.530	-2.408	Type IN
1-179561	8615	1902	319.751	-0.964	0.020	10.020	-0.113	Type IN
1-26197	8652	6102	330.724	-0.785	0.064	11.130	-3.828	Type IN
1-188530	8995	3703	175.818	55.278	0.055	10.780	-4.158	Type IN
1-323766	9027	1902	246.176	32.064	0.022	9.900	-2.393	Type IN
1-295839	9047	3703	247.072	25.704	0.131	11.430	-3.293	Type IN
1-109275	9192	3703	46.071	0.520	0.044	10.060	-0.308	Type IN
1-42247	9514	1902	33.588	14.119	0.029	9.710	-0.143	Type IN
1-42082	9514	3701	32.825	12.922	0.060	10.880	-4.073	Type IN
1-593328	9868	12704	219.657	46.663	0.037	nan	nan	Type IN
1-633000	9872	3701	233.232	42.438	0.020	10.110	-0.103	Type IN
1-389466	10838	1902	147.550	34.699	0.038	10.090	-0.028	Type IN
1-245235	11012	3702	211.425	55.777	0.041	10.150	0.022	Type IN
1-13736	11834	1902	223.081	-0.269	0.044	10.080	-0.453	Type IN
1-22347	7992	3701	252.171	63.479	0.044	10.430	-4.513	Type CT
1-339061	8138	6102	117.144	44.688	0.020	10.410	-4.093	Type CT
1-38543	8155	3702	54.032	-0.596	0.023	10.500	-4.428	Type CT
1-199775	8314	3702	240.848	39.986	0.030	10.170	-0.063	Type CT
1-284335	8318	6103	196.821	45.728	0.035	9.840	-4.873	Type CT
1-251198	8332	3704	209.640	41.724	0.043	10.220	-0.453	Type CT
1-419257	8444	3701	201.141	31.546	0.023	10.260	-0.823	Type CT
1-418253	8446	1902	206.154	37.172	0.027	10.650	-4.278	Type CT
1-210611	8600	1902	244.391	41.689	0.027	nan	nan	Type CT
1-379008	8711	1902	118.761	52.227	0.023	9.710	-1.063	Type CT
1-71956	8713	3704	118.442	38.869	0.040	9.830	-2.323	Type CT
1-188177	8991	6103	176.130	53.683	0.027	10.430	-4.498	Type CT
1-149871	8992	3704	173.487	51.250	0.026	10.840	-4.108	Type CT
1-94690	9026	3704	251.378	43.582	0.031	10.310	-0.853	Type CT
1-94773	9026	1902	249.302	44.086	0.033	10.180	-1.448	Type CT
1-295542	9048	1902	246.256	24.263	0.050	10.450	0.737	Type CT
1-178027	9186	3704	258.743	29.138	0.045	10.540	-4.333	Type CT
1-382889	9496	3701	120.620	20.514	0.029	10.580	-1.043	Type CT
1-153127	10220	1901	120.805	33.132	0.018	9.880	-4.903	Type CT
1-76425	10511	3704	131.828	2.762	0.028	10.760	-4.153	Type CT
1-77006	10512	1902	135.588	3.616	0.024	10.030	-1.748	Type CT
1-151874	11019	1901	192.363	51.582	0.032	10.380	-2.628	Type CT
1-244115	11020	1901	204.506	55.188	0.025	10.380	-3.183	Type CT
1-586725	11838	3704	156.032	0.142	0.023	nan	nan	Type CT
1-135190	11942	3702	246.753	40.811	0.030	10.630	-4.298	Type CT
1-294016	11981	1901	254.321	19.339	0.033	9.560	-0.628	Type CT
1-386932	12487	1902	137.844	30.096	0.026	9.740	-0.413	Type CT

1-41258	8093	3703	22.175	14.609	0.036	10.870	-4.073	Type OUT
1-44483	8143	3702	119.835	42.057	0.025	10.320	-4.618	Type OUT
1-44047	8143	1902	119.643	41.578	0.041	10.260	-3.843	Type OUT
1-232087	8152	3703	142.725	35.440	0.028	10.390	-4.563	Type OUT
1-251067	8332	3703	207.478	43.482	0.045	10.380	-4.533	Type OUT
1-266244	8333	1902	216.547	42.711	0.017	9.010	-0.743	Type OUT
1-136248	8606	3702	253.794	36.906	0.024	10.580	-3.688	Type OUT
1-248410	8979	3701	241.209	42.036	0.025	9.660	-0.753	Type OUT
1-174947	8989	9101	176.359	49.879	0.033	10.700	-2.998	Type OUT
1-269003	9032	1902	242.045	31.515	0.014	9.750	-4.998	Type OUT
1-78381	10515	12702	148.003	4.151	0.031	11.090	-3.848	Type OUT
1-245301	11012	6104	212.532	54.920	0.040	10.880	-4.038	Type OUT
1-566335	11962	3701	226.283	8.107	0.047	nan	nan	Type OUT
1-40771	12093	3701	17.785	14.223	0.054	11.280	-3.653	Type OUT
1-113520	7815	1901	317.502	11.511	0.017	9.970	-4.998	Type MIS
1-519907	8310	1901	179.645	24.117	0.030	10.130	-4.198	Type MIS
1-418023	8446	1901	205.753	36.166	0.024	nan	nan	Type MIS
1-248869	8604	6103	244.691	39.334	0.032	11.020	-3.923	Type MIS
1-635506	8618	6102	319.103	10.273	0.017	10.200	-1.618	Type MIS
1-163594	8726	1901	115.494	23.176	0.043	11.140	-2.493	Type MIS
1-235983	8980	3701	223.636	42.385	0.018	9.860	-4.998	Type MIS
1-246484	9865	1902	223.866	51.048	0.030	9.910	-4.968	Type MIS
1-4109	12491	1901	166.240	1.038	0.043	10.130	-0.653	Type MIS
1-145871	8148	3702	118.531	27.692	0.065	11.060	-3.903	Type NO-EML
1-37478	8154	1902	44.847	-1.167	0.028	10.560	-3.998	Type NO-EML
1-196580	8309	6102	208.508	51.905	0.144	11.550	-3.418	Type NO-EML
1-250784	8327	1902	202.961	44.152	0.034	10.910	-2.708	Type NO-EML
1-251783	8335	1901	215.311	39.653	0.026	10.240	-1.993	Type NO-EML
1-166613	8461	3701	144.516	42.974	0.047	11.140	-2.473	Type NO-EML
1-90192	8553	6102	233.713	56.451	0.039	11.220	-1.153	Type NO-EML
1-95120	8601	9102	250.406	40.163	0.034	11.250	-3.618	Type NO-EML
1-210728	8604	3701	247.280	39.496	0.029	10.490	-4.448	Type NO-EML
1-635590	8615	3702	321.054	1.118	0.049	nan	nan	Type NO-EML
1-44113	8718	3701	120.206	44.691	0.102	11.610	-3.358	Type NO-EML
1-456904	8933	3703	195.184	28.337	0.026	10.570	-2.743	Type NO-EML
1-279554	8945	3701	171.628	46.998	0.025	10.530	-4.298	Type NO-EML
1-624035	8949	3703	195.875	28.275	0.021	9.560	-4.998	Type NO-EML
1-278079	8993	3704	166.087	46.056	0.143	11.510	-3.403	Type NO-EML
1-188165	8995	3704	175.602	54.774	0.058	11.400	-3.558	Type NO-EML
1-269227	9028	1901	242.670	30.255	0.031	10.570	-4.368	Type NO-EML
1-135244	9029	3703	246.907	42.638	0.031	10.880	-3.228	Type NO-EML
1-593972	9042	3703	235.202	28.292	0.033	nan	nan	Type NO-EML
1-50956	9188	3702	48.523	-8.457	0.034	10.940	-3.798	Type NO-EML
1-603965	9194	3701	46.885	-0.965	0.039	11.380	-1.028	Type NO-EML
1-387045	9505	1902	139.777	27.915	0.028	9.810	-2.578	Type NO-EML
1-623416	9873	12703	194.475	28.500	0.024	10.240	-4.293	Type NO-EML
1-456672	9874	12705	195.080	27.554	0.020	10.260	-4.678	Type NO-EML
1-456884	9875	9101	194.580	27.762	0.018	9.570	-4.538	Type NO-EML
1-316773	9888	3702	235.375	27.987	0.032	11.070	-3.823	Type NO-EML

1-297863	10216	1902	116.767	18.138	0.045	10.280	-1.793	Type NO-EML
1-280716	10507	3703	177.397	47.831	0.025	10.480	-4.263	Type NO-EML
1-182730	10519	3704	154.598	5.736	0.074	11.120	-3.758	Type NO-EML
1-762	10843	3704	149.655	-0.930	0.061	11.420	-3.513	Type NO-EML
1-320459	11016	6102	210.887	49.969	0.071	11.450	-3.533	Type NO-EML
1-559761	11022	3701	218.935	4.993	0.030	nan	nan	Type NO-EML
1-83002	11835	9102	221.318	3.404	0.028	10.610	-3.973	Type NO-EML
1-283130	11953	3701	189.060	42.637	0.028	9.800	-2.003	Type NO-EML
1-333770	11962	6103	226.307	8.797	0.045	11.110	-3.058	Type NO-EML
1-632581	11967	3701	230.913	8.759	0.034	10.920	-3.993	Type NO-EML
1-591742	12620	1901	201.115	30.978	0.023	nan	nan	Type NO-EML
1-135772	12667	3703	250.386	37.266	0.101	11.420	-3.528	Type NO-EML

(1) MaNGA-ID; (2) Plate; (3) IFU; (4) Right Ascension; (5) Declination; (6) Redshift; (7) Stellar mass; (8) Star formation rate; (9) Classification of the CRD galaxies based on their stellar and gas kinematics.

Acknowledgements: M.B. acknowledges support by the National Natural Science Foundation of China, NSFC grants No. 12541302 and No. 12303009. Y.M.C. acknowledges support by NSFC grant No. 12333002, the China Manned Space Project No. CMS-CSST-2025-A08 and the Fundamental Research Funds for the Central Universities No. KG202502. Funding for the Sloan Digital Sky Survey IV has been provided by the Alfred P. Sloan Foundation, the U.S. Department of Energy Office of Science, and the Participating Institutions. SDSS-IV acknowledges support and resources from the Center for High-Performance Computing at the University of Utah. The SDSS web site is www.sdss.org. SDSS-IV is managed by the Astrophysical Research Consortium for the Participating Institutions of the SDSS Collaboration including the Brazilian Participation Group, the Carnegie Institution for Science, Carnegie Mellon University, the Chilean Participation Group, the French Participation Group, Harvard-Smithsonian Center for Astrophysics, Instituto de Astrofísica de Canarias, The Johns Hopkins University, Kavli Institute for the Physics and Mathematics of the Universe (IPMU) / University of Tokyo, Lawrence Berkeley National Laboratory, Leibniz Institut für Astrophysik Potsdam (AIP), Max-Planck-Institut für Astronomie (MPIA Heidelberg), Max-Planck-Institut für Astrophysik (MPA Garching), Max-Planck-Institut für Extraterrestrische Physik (MPE), National Astronomical Observatory of China, New Mexico State University, New York University, University of Notre Dame, Observatório Nacional / MCTI, The Ohio State University, Pennsylvania State University, Shanghai Astronomical Observatory, United Kingdom Participation Group, Universidad Nacional Autónoma de México, University of Arizona, University of Colorado Boulder, University of Oxford, University of Portsmouth, University of Utah, University of Virginia, University of Washington, University of Wisconsin, Vanderbilt University, and Yale University.

REFERENCES

- Abdurro'uf, Accetta, K., Aerts, C., et al. 2022, *ApJS*, 259, 35. doi:10.3847/1538-4365/ac4414
- Argudo-Fernández, M., Verley, S., Bergond, G., et al. 2015, *A&A*, 578, A110. doi:10.1051/0004-6361/201526016
- Bao, M., Chen, Y., Zhu, P., et al. 2022, *ApJL*, 926, L13. doi:10.3847/2041-8213/ac52ad
- Bao, M., Chen, Y., Gu, Q., et al. 2025, *ApJL*, 982, 1, L29. doi:10.3847/2041-8213/adbc68
- Barrera-Ballesteros, J. K., García-Lorenzo, B., Falcón-Barroso, J., et al. 2015, *A&A*, 582, A21. doi:10.1051/0004-6361/201424935
- Barrera-Ballesteros, J. K., Utomo, D., Bolatto, A. D., et al. 2020, *MNRAS*, 492, 2651. doi:10.1093/mnras/stz3553
- Bevacqua, D., Cappellari, M., & Pellegrini, S. 2022, *MNRAS*, 511, 139. doi:10.1093/mnras/stab3732
- Blanton, M. R., Kazin, E., Muna, D., et al. 2011, *AJ*, 142, 31. doi:10.1088/0004-6256/142/1/31
- Blanton, M. R., Bershad, M. A., Abolfathi, B., et al. 2017, *AJ*, 154, 28. doi:10.3847/1538-3881/aa7567
- Blumenthal, G. R., Faber, S. M., Primack, J. R., et al. 1984, *Nature*, 311, 517. doi:10.1038/311517a0
- Braun, R., Waltherbos, R. A. M., Kennicutt, R. C., et al. 1994, *ApJ*, 420, 558. doi:10.1086/173586
- Bryant, J. J., Croom, S. M., van de Sande, J., et al. 2019, *MNRAS*, 483, 458. doi:10.1093/mnras/sty3122

- Cao, X., Chen, Y.-M., Shi, Y., et al. 2022, *Nature Astronomy*, 6, 1464. doi:10.1038/s41550-022-01788-8
- Cao, Y. & Pan, Z. 2025, *ApJ*, 992, 2, 169. doi:10.3847/1538-4357/ae0a10
- Cappellari, M. & Emsellem, E. 2004, *PASP*, 116, 816, 138. doi:10.1086/381875
- Cappellari, M., Emsellem, E., Krajnović, D., et al. 2011, *MNRAS*, 413, 2, 813. doi:10.1111/j.1365-2966.2010.18174.x
- Cappellari, M. 2017, *MNRAS*, 466, 1, 798. doi:10.1093/mnras/stw3020
- Chang, Y.-Y., van der Wel, A., da Cunha, E., et al. 2015, *ApJS*, 219, 8. doi:10.1088/0067-0049/219/1/8
- Chen, Y.-M., Shi, Y., Tremonti, C. A., et al. 2016, *Nature Communications*, 7, 13269. doi:10.1038/ncomms13269
- Chen, Y.-Y., Chen, Y.-M., Gu, Q.-S., et al. 2019, *Research in Astronomy and Astrophysics*, 19, 6, 081. doi:10.1088/1674-4527/19/6/81
- Cocato, L., Morelli, L., Corsini, E. M., et al. 2011, *MNRAS*, 412, L113. doi:10.1111/j.1745-3933.2011.01016.x
- Cocato, L., Morelli, L., Pizzella, A., et al. 2013, *A&A*, 549, A3. doi:10.1051/0004-6361/201220460
- Conselice, C. J. & Arnold, J. 2009, *MNRAS*, 397, 208. doi:10.1111/j.1365-2966.2009.14959.x
- Corsini, E. M., Pizzella, A., & Bertola, F. 2002, *A&A*, 382, 488. doi:10.1051/0004-6361:20011647
- Corsini, E. M. 2014, *Multi-Spin Galaxies*, 486, 51. doi:10.48550/arXiv.1403.1263
- Croom, S. M., Lawrence, J. S., Bland-Hawthorn, J., et al. 2012, *MNRAS*, 421, 1, 872. doi:10.1111/j.1365-2966.2011.20365.x
- Dalcanton, J. J. 2007, *ApJ*, 658, 2, 941. doi:10.1086/508913
- Davis, T. A., Alatalo, K., Sarzi, M., et al. 2011, *MNRAS*, 417, 882. doi:10.1111/j.1365-2966.2011.19355.x
- Diemand, J., Kuhlen, M., & Madau, P. 2007, *ApJ*, 667, 859. doi:10.1086/520573
- Dopita, M. A., Kewley, L. J., Sutherland, R. S., et al. 2016, *Ap&SS*, 361, 61. doi:10.1007/s10509-016-2657-8
- Drory, N., MacDonald, N., Bershady, M. A., et al. 2015, *AJ*, 149, 77. doi:10.1088/0004-6256/149/2/77
- Duckworth, C., Tojeiro, R., & Kraljic, K. 2020, *MNRAS*, 492, 2, 1869. doi:10.1093/mnras/stz3575
- Fall, S. M. & Efstathiou, G. 1980, *MNRAS*, 193, 189. doi:10.1093/mnras/193.2.189
- Fisher, D., Illingworth, G., & Franx, M. 1994, *AJ*, 107, 160. doi:10.1086/116841
- Fischer, J.-L., Domínguez Sánchez, H., & Bernardi, M. 2019, *MNRAS*, 483, 2, 2057. doi:10.1093/mnras/sty3135
- Gasymov, D., Katkov, I. Y., Rubtsov, E. V., et al. 2025, , arXiv:2504.02925. doi:10.48550/arXiv.2504.02925
- Genel, S., Bouché, N., Naab, T., et al. 2010, *ApJ*, 719, 229. doi:10.1088/0004-637X/719/1/229
- Gunn, J. E., Siegmund, W. A., Mannery, E. J., et al. 2006, *AJ*, 131, 2332. doi:10.1086/500975
- Healy, J., de Blok, W. J. G., & Maccagni, F. M. 2023, *Resolving the Rise and Fall of Star Formation in Galaxies*, 373, 124. doi:10.1017/S1743921322004264
- Hunter, D. A., van Woerden, H., & Gallagher, J. S. 1999, *AJ*, 118, 2184. doi:10.1086/301096
- Jin, Y., Chen, Y., Shi, Y., et al. 2016, *MNRAS*, 463, 913. doi:10.1093/mnras/stw2055
- Kashino, D., Renzini, A., Silverman, J. D., et al. 2016, *ApJL*, 823, 2, L24. doi:10.3847/2041-8205/823/2/L24
- Katkov, I. Y., Sil'chenko, O. K., Chilingarian, I. V., et al. 2016, *MNRAS*, 461, 2068. doi:10.1093/mnras/stw1452
- Kauffmann, G., Li, C., & Heckman, T. M. 2010, *MNRAS*, 409, 491. doi:10.1111/j.1365-2966.2010.17337.x
- Kewley, L. J. & Dopita, M. A. 2002, *ApJS*, 142, 1, 35. doi:10.1086/341326
- Krajnović, D., Cappellari, M., de Zeeuw, P. T., et al. 2006, *MNRAS*, 366, 787. doi:10.1111/j.1365-2966.2005.09902.x
- L'Huillier, B., Combes, F., & Semelin, B. 2012, *A&A*, 544, A68. doi:10.1051/0004-6361/201117924
- Li, S.-. lin ., Shi, Y., Bizyaev, D., et al. 2021, *MNRAS*, 501, 14. doi:10.1093/mnras/staa3618
- Liu, Y. & Lan, M.-X. 2026, *ApJ*, 997, 1, 54. doi:10.3847/1538-4357/ae2fb3
- Lu, S., Xu, D., Wang, Y., et al. 2021, *MNRAS*, 503, 1, 726. doi:10.1093/mnras/stab497
- Maccagni, F. M., Morganti, R., Oosterloo, T. A., et al. 2014, *A&A*, 571, A67. doi:10.1051/0004-6361/201424334
- Mitzkus, M., Cappellari, M., & Walcher, C. J. 2017, *MNRAS*, 464, 4789. doi:10.1093/mnras/stw2677
- Morganti, R., Peck, A. B., Oosterloo, T. A., et al. 2009, *A&A*, 505, 2, 559. doi:10.1051/0004-6361/200912605
- Pan, Z., Li, J., Lin, W., et al. 2014, *ApJL*, 792, L4. doi:10.1088/2041-8205/792/1/L4
- Pizzella, A., Morelli, L., Corsini, E. M., et al. 2014, *A&A*, 570, A79. doi:10.1051/0004-6361/201424746
- Pizzella, A., Morelli, L., Cocato, L., et al. 2018, *A&A*, 616, A22. doi:10.1051/0004-6361/201731712
- Plana, H. & Boulesteix, J. 1996, *A&A*, 307, 391
- Ristea, A., Cortese, L., Fraser-McKelvie, A., et al. 2022, *MNRAS*, 517, 2, 2677. doi:10.1093/mnras/stac2839
- Rubin, V. C., Graham, J. A., & Kenney, J. D. P. 1992, *ApJL*, 394, L9. doi:10.1086/186460
- Sancisi, R., Fraternali, F., Oosterloo, T., et al. 2008, *A&A Rv*, 15, 3, 189. doi:10.1007/s00159-008-0010-0

- Sánchez, S. F., Kennicutt, R. C., Gil de Paz, A., et al. 2012, *A&A*, 538, A8. doi:10.1051/0004-6361/201117353
- Sánchez Almeida, J., Elmegreen, B. G., Muñoz-Tuñón, C., et al. 2014, *A&A Rv*, Star formation sustained by gas accretion, 22, 71. doi:10.1007/s00159-014-0071-1
- Sánchez-Blázquez, P., Peletier, R. F., Jiménez-Vicente, J., et al. 2006, *MNRAS*, 371, 2, 703. doi:10.1111/j.1365-2966.2006.10699.x
- Sánchez, S. F., Barrera-Ballesteros, J. K., Lacerda, E., et al. 2022, *ApJS*, 262, 2, 36. doi:10.3847/1538-4365/ac7b8f
- Santana, K. C., Maccagni, F. M., Deane, R. P., et al. 2025, *MNRAS*, 540, 3, 2396. doi:10.1093/mnras/staf832
- Sarzi, M., Iodice, E., Cocato, L., et al. 2018, *A&A*, 616, A121. doi:10.1051/0004-6361/201833137
- Smirnova-Pinchukova, I., Husemann, B., Davis, T. A., et al. 2022, *A&A*, 659, A125. doi:10.1051/0004-6361/202142011
- Smee, S. A., Gunn, J. E., Uomoto, A., et al. 2013, *AJ*, 146, 32. doi:10.1088/0004-6256/146/2/32
- Tillson, H., Miller, L., & Devriendt, J. 2011, *MNRAS*, 417, 666. doi:10.1111/j.1365-2966.2011.19311.x
- Wang, J., Navarro, J. F., Frenk, C. S., et al. 2011, *MNRAS*, 413, 1373. doi:10.1111/j.1365-2966.2011.18220.x
- Wake, D. A., Bundy, K., Diamond-Stanic, A. M., et al. 2017, *AJ*, 154, 86. doi:10.3847/1538-3881/aa7ecc
- Westfall, K. B., Cappellari, M., Bershady, M. A., et al. 2019, *AJ*, 158, 231. doi:10.3847/1538-3881/ab44a2
- Yan, R., Chen, Y., Lazarz, D., et al. 2019, *ApJ*, 883, 2, 175. doi:10.3847/1538-4357/ab3ebc
- Zhou, Y., Chen, Y., Shi, Y., et al. 2022, *MNRAS*, 515, 5081. doi:10.1093/mnras/stac2016